Journal of Environmental Chemical Engineering 13 (2025) 115542

Contents lists available at ScienceDirect

Journal of Environmental Chemical Engineering

journal homepage: www.elsevier.com/locate/jece

Constructing highly effective CuS/In_2S_3 Z-scheme heterojunction with boosted charge transfer for enhanced photocatalytic performance

Tingting Yang [a], Bin Wang [a,b,*], Xingwang Yan [a], Gaopeng Liu [a], Junze Zhao [a], Mengxia Ji [a], Paul K. Chu [b], Jiexiang Xia [a,**], Huaming Li [a,**]

[a] School of Chemistry and Chemical Engineering, Institute for Energy Research, Jiangsu University, 301 Xuefu Road, Zhenjiang 212013, China
[b] Department of Physics, Department of Materials Science and Engineering, and Department of Biomedical Engineering, City University of Hong Kong, Tat Chee Avenue, Kowloon, Hong Kong

ARTICLE INFO

Keywords:
CuS/In_2S_3
Z-scheme heterojunction
Photocatalysis
Pollutants degradation

ABSTRACT

Semiconductor photocatalysis technology is a promising technique for the environmental remediation and new energy development. It is of importance to design the photocatalysts with wide spectral response, high carrier separation efficiency and high redox capacity for the photocatalysis. Herein, a CuS/In_2S_3 Z-scheme heterojunction is designed and constructed by a one-step hydrothermal method. UPS, free radicals trapping experiments and ESR confirm that the electrons are transferred from CuS to In_2S_3 through the Z-Scheme mechanism. Benefiting from the construction of Z-scheme heterostructure, the separation of photogenerated carriers is more effective and the redox capacity of the pristine materials reserves the maximum. Compared to pure CuS and In_2S_3, CuS/ In_2S_3-4 represents the best photocatalytic performance boosting degradation rates of MBT that are 28.1 and 21.7 times higher than this of the CuS and In_2S_3, respectively. In the photocatalytic process, $\cdot O_2^-$ and h^+ are the main active species. Bean sprout planting experiment showed that the toxicity of the solution decreased after degradation. This work provides a new method of constructing a high-performance Z-scheme heterojunction material for improving the activity and efficiency of the photocatalysts.

1. Introduction

Due to the fast development of economy and industry, energy shortage and environmental pollution have become the key problems to be solved urgently [1,2]. The water pollution by organic pollutants has become one of the biggest environmental challenges [3–5]. Among the pollutants, MBT is a kind of mercaptan which is extensively used as a raw material in many chemical production [6]. However, its heterocyclic structure containing nitrogen and sulfur poses a highly toxic threat to

the environment and human safety [7,8]. Especially when it is over discharged into the water, it will cause the chemical characteristics of the water to change which will affect the effective use of water resulting in the deterioration of water quality [9]. As a kind of advanced oxidation technology, semiconductor photocatalysis has potential application value in the fields of environmental remediation and new energy development [10–12]. Among the most proposed photocatalysts, such as TiO_2 [13] and ZnO [14] only can generate carriers under the excitation of the ultraviolet light, which is a huge obstacle for their industrial application. And as for the carbon nitride [15,16] and bismuth halide oxide [17], the rapid recombination of photo-induced electron-hole pairs also limits their application. Therefore, improving the utilization of the solar energy, the separation of photo-generated carriers and the redox capacity of the photocatalysts are the key to strengthen the application of semiconductor photocatalysis technology [18–20].

The construction of suitable heterojunctions is one of the methods to improve the effective segregation of photogenerated carriers in catalysts. Wu et al.[21] proposed and constructed a type-I C_3N_4-based isotype heterojunction which displayed high H_2O_2 yield, outstanding utilization efficiency and excellent degradation performance. Ding et al. [22] proposed a CdS/NiS type II heterojunction which achieved a good photocatalytic hydrogen evolution reaction (HER) performance. Although the construction of type I and type II heterojunctions can effectively separate the photogenerated electron hole pairs of the

* Corresponding author at: School of Chemistry and Chemical Engineering, Institute for Energy Research, Jiangsu University, 301 Xuefu Road, Zhenjiang 212013, China.
** Corresponding authors.
E-mail addresses: wangbin@ujs.edu.cn (B. Wang), xjx@ujs.edu.cn (J. Xia), lhm@ujs.edu.cn (H. Li).

https://doi.org/10.1016/j.jece.2025.115542
Received 11 October 2024; Received in revised form 17 December 2024; Accepted 19 January 2025
Available online 20 January 2025

catalysts, the redox ability is weak. Xia et al.[23] designed a $ZnIn_2S_4$/-$BiVO_4$ Z-scheme heterojunction to effective separate photogenerated carriers and maintain the robust redox ability in the materials to enhance the ability of antibiotic degradation. Hence, constructing Z-scheme heterojunction can restrain the recombination of photogenerated electron and hole pairs and retain the original redox ability of the photocatalysts to improve the photocatalytic performance [24–26].

Recently, indium sulfide (In_2S_3) has become a research hotpot because of its low toxicity and suitable and adjustable band structure. It is considered as a promising catalyst for photocatalytic origin pollutants degradation [27], CO_2 reduction [28], H_2 production [29], N_2 fixation [30] and so on. However, the recombination of charge carriers of In_2S_3 is fast and it will be photocorroded in the process of degradation [31–34]. Therefore, different strategies have been proposed to improve the photocatalytic efficiency of In_2S_3, such as controlling the morphology$_3$, doping metals or nonmetals, using cocatalysts and forming complexes [35,36]. Copper sulfide (CuS) has caused great interests in photocatalysis because of its wide light absorption range and no secondary pollution. The energy bands of CuS and In_2S_3 are crossed. It is expected to construct Z-scheme heterojunction to further improve the migration and separation efficiency of the photogenerated carriers of the materials, and maintain the high oxidation/reduction performance of the material. Therefore, the combination of In_2S_3 with CuS may be a promising photocatalyst for the photocatalysis. However, to our knowledge, there have been no reports of degradation with CuS/In_2S_3 composites.

In this work, CuS/In_2S_3 Z-scheme heterojunction is designed and fabricated through solvothermal and hydrothermal method. The construction of the Z-scheme heterojunction not only enhances the separation of carriers but also achieves high redox capability. Among the materials, CuS/In_2S_3-4 has the best photocatalytic properties and the degradation rate of 2-mercaptobenzothiazole (MBT) is 21.7 and 28.1 times than In_2S_3 and CuS, respectively. The cultivation of bean sprouts showed that the toxicity of the solution after degradation was very low. Our combined analysis proves CuS/In_2S_3-4 produces the highest surface photogenerated electron and hole concentrations. The results and mechanism are discussed.

2. Experimental details

2.1. Materials and synthesis

Indium chloride tetrahydrate ($InCl_3 \cdot 4\ H_2O$) was bought from Shanghai Aladdin Biochemical Technology Co., Ltd. Urea (CH_4N_2O), Copper(II) nitrate trihydrate

($Cu(NO_3)_2 \cdot 3\ H_2O$) and thiourea (CH_4N_2S) were bought from Sinopharm Group Chemical Reagent Co., Ltd. And the purity of the chemicals is classified as analytical grade. Scheme 1 demonstrates the synthesis of the In_2S_3 and CuS/In_2S_3.

2.1.1. Synthesis of $In(OH)_3$

Dissolved 1.7 mmol $InCl_3 \cdot 4\ H_2O$ and 67 mmol urea into 45 mL deionized water and stirred 30 minutes. Then shifted the clarified solution into a 50 mL flask and heated at 80 °C 2 hours. Finally, After washing it with distilled water and dried at 40 °C, white $In(OH)_3$ was obtained.

2.1.2. Synthesis of In_2S_3

Dissolved 4.0 mmol thiourea in 20 mL anhydrous ethanol, then 0.60 mmol $In(OH)_3$ was added before sonication and stirred 30 minutes. The solvothermal reaction was then carried out at 180 °C for 24 hours. After washing it with distilled water and anhydrous ethanol and dried at 40 °C, yellow In_2S_3 was obtained.

2.1.3. Synthesis of CuS

Dissolved 12 mmol thiourea and 0.6 mmol $Cu(NO_3)_2 \cdot 3\ H_2O$ in 30 mL deionized water and stirred 30 minutes. The hydrothermal reaction was then carried out at 160 °C for 6 hours. After washing it with distilled water and anhydrous ethanol and dried at 60 °C, the black CuS was obtained.

2.1.4. Synthesis of CuS/In_2S_3

A certain amount of $Cu(NO_3)_2 \cdot 3\ H_2O$ (0.01 g, 0.02 g, 0.03 g and 0.04 g) was dissolved in 30 mL distilled water. 0.10 g In_2S_3 was added to the solution and stirred for 30 min. The hydrothermal reaction was then carried out at 160 °C for 6 hours. After washing it with distilled water and anhydrous ethanol and dried at 40 °C, the CuS/In_2S_3-2, CuS/In_2S_3-4, CuS/In_2S_3-6, and CuS/In_2S_3-8 were obtained.

2.2. Materials characterization

Using the scanning electron microscopy (SEM, JOEL JSM-7800F), transmission electron microscopy (TEM, JEM 2100 F FEI Tecnai F20/F30), and high-resolution transmission electron microscopy (HR-TEM, JEM 2100 F FEI Tecnai F20/F30) to observe the morphology of the materials. The Shimadzu XRD-6000X-ray diffractometer with Cu Kα irradiation was used to measure X-ray diffraction (XRD) of the materials and UV-3600 Plus spectrophotometer (Shimadzu Corporation, Japan) was used for determining UV–vis diffuse reflectance spectra (UV–vis DRS). X-ray photoelectron spectroscopy (XPS, ESCALAB QXi) was carried out to determine the surface chemical compositions and chemical valence states. The molecules produced during MBT decomposition were measured by the mass spectrometry (MS) (ThermoLXQ LC/MS). The specific surface area and particle size of the photocatalysts were determined using a specific surface area analyzer (Micromeritics Instrument Corporation, USA). Using Na_2SO_4 (0.2 M) and a 10 W Xe lamp to test the photocurrent. The Mott-Schottky (M-S) was performed at an electrochemical station (Chenhua Instruments Company) at 1 M KCl by means of an electrochemical device with the standard 3-electrode configuration. The work function of samples was obtained by Ultraviolet Photoelectron Spectroscopy (UPS; ESCALAB QXi) with a He I (21.2 eV) photon source. The photoluminescence (PL, QM4m) spectra occurred at an excitation wavelength of 360 nm. Electron spin resonance (ESR) from Bruker JES-FA200 spectrometer to measure hyperoxidized under light conditions.

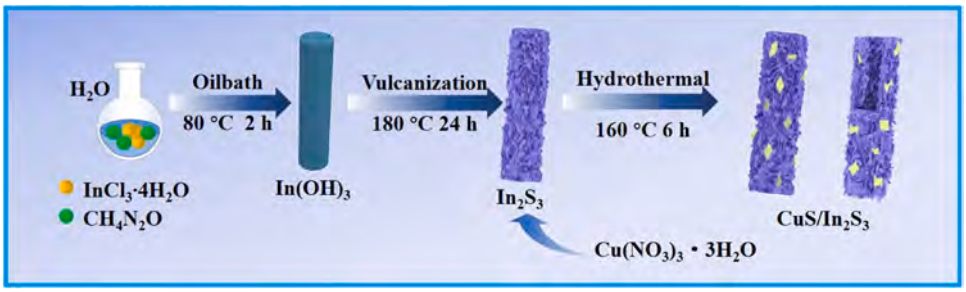

Scheme 1. Schematic illustration of the synthesis of the CuS/In_2S_3.

2.3. Photocatalytic experiments

Dispersed 50 mg of photocatalysts in 100 mL MBT solution (10 mg L^{-1}). Using a circulating water system to keep the temperature at 20 ℃. In order to have sufficient oxygen during the reaction, air is pumped into the reactor. A 250 W Xe lamp with a 420 nm filter was used as the light source. Before light exposure, stirred the suspension 30 min to establish adsorption and desorption equilibrium. In the photocatalytic process, every 15 minutes about 4 mL suspension was extracted and centrifuged. The absorbance of 2-mercaptobenzothiazole (MBT) was measured at 320 nm and the performance of the materials were measured according to the absorbance.

3. Results and discussion

3.1. Structure and morphology characterization of catalysts

The monographic of the materials was observed by SEM and TEM. As shown in Fig. 1a-b, In_2S_3 shows hollow tubular structure decorated nanosheets 1.2 μm in length and 200 nm in diameter. Fig. 1d-e shows the morphology of CuS. It shows a flower-like sphere structure with an average diameter of 4 μm which self-assembled by nanosheets. The SEM and TEM images of CuS/In_2S_3 are shown in Fig. 1**g-h, S1 and S2**, the CuS nanosheets are dispersed on the surface of the In_2S_3 hollow tubular. And with the amount of the $Cu(NO_3)_2{\cdot}3\,H_2O$ added increases, the CuS nanosheets on the surface of In_2S_3 increases. HR-TEM was carried out to observe the microstructure of photocatalysts, the lattice spacing of 0.31 nm indexed to the (2 2 2) crystal facet of In_2S_3, while the 0.32 nm lattice spacing derived from the (2 0 3) crystal plane of CuS (Fig. 1c, f, i). The crystal facets of In_2S_3 and CuS are staggered arrangement revealing the successful formation of the heterojunction. The TEM-EDS maps (Fig. 1j) and line scan spectra (Fig. S3) of CuS/In_2S_3-4 in demonstrates the existence of three elements: In, Cu and S in CuS/In_2S_3 composites.

The nitrogen adsorption-desorption isotherms are depicted in Fig. 2a, the specific surface areas of In_2S_3, CuS and CuS/In_2S_3-4 are 101.8, 0.1 and 34.5 $m^2{\cdot}g^{-1}$, respectively. CuS nanosheets fill part of the

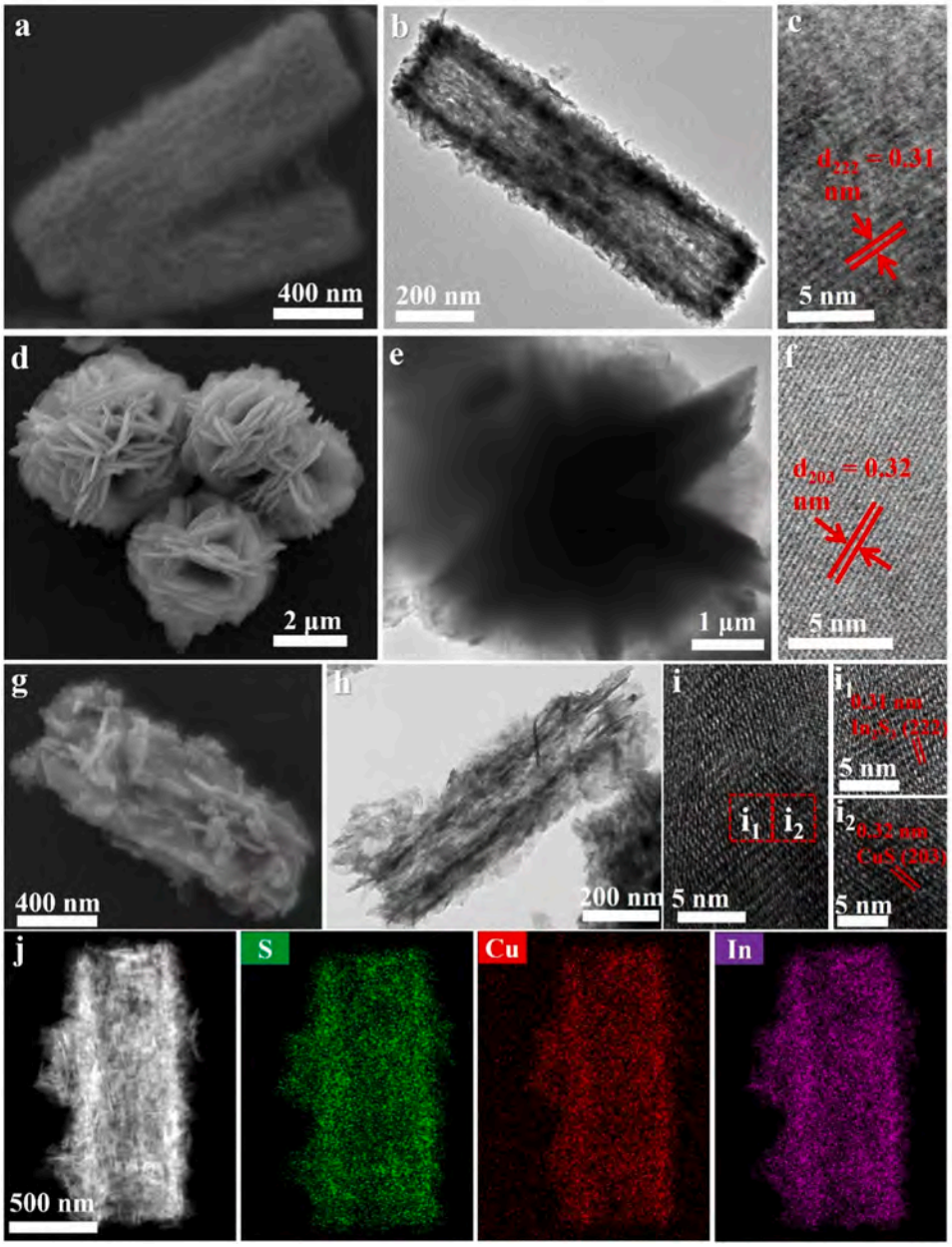

Fig. 1. SEM and TEM images of (a, b) In_2S_3, (d, e) CuS, (g, h) CuS/In_2S_3-4; HR-TEM images of (c) In_2S_3, (f) CuS, (i) CuS/In_2S_3-4; (j) element maps of CuS/In_2S_3-4.

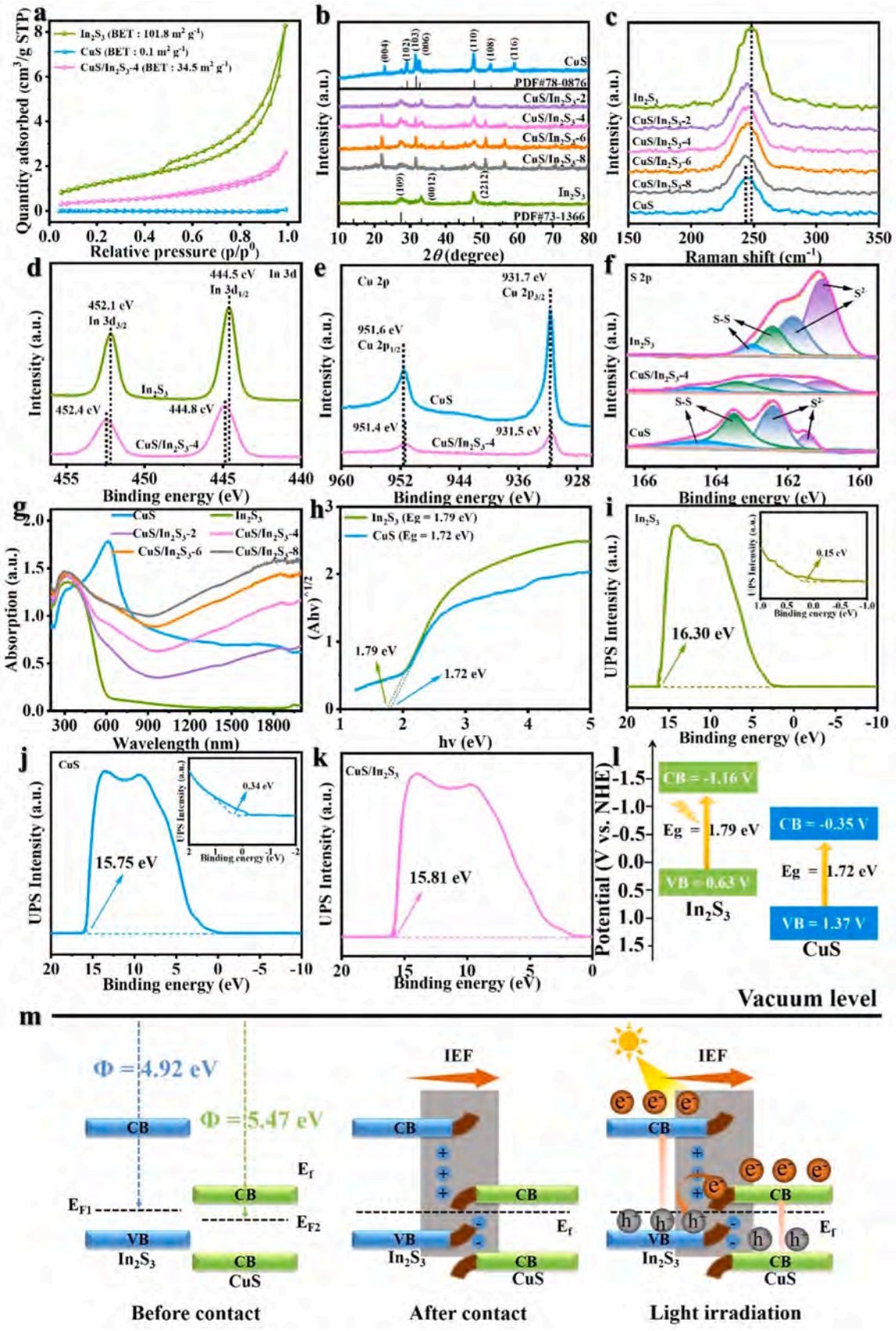

Fig. 2. (a) N_2 adsorption-desorption isotherms; (b) XRD patterns; (c) Raman spectra; (d, e, f) XPS In 3*d*, Cu 2*p* and S 2*p* spectra; (g) UV–vis DRS; (h) bandgaps; (i-k) UPS spectra; (l) band structure of In_2S_3, CuS and CuS/In_2S_3; (m) band arrangement and charge transfer paths of In_2S_3 and CuS before contact, after dark contact and under light contact.

voids on the surface of In2S3 hollow tubes, resulting in a smaller specific surface area of the composite material than that of In_2S_3, which is consistent with the characterization results of SEM and TEM. The XRD patterns of In_2S_3, CuS and CuS/In_2S_3 are shown in Fig. 2b. Pure In_2S_3 has three strong peaks at 27.4°, 33.2° and 47.7°, which correspond to the (1 0 9), (0 0 12) and (2 2 12) diffraction surfaces of tetragonal In_2S_3 phase (JCPDS No. 73–1366). The XRD pattern of CuS is similar to the hexagonal phase of CuS (JCPDS NO. 78–0876), and the peaks at 21.7°, 29.2°, 31.7°, 32.8° and 47.9° correspond to the facets of (0 0 4), (1 0 2), (1 0 3), (0 0 6) and (1 1 0) of CuS. No impurities are observed by XRD in In_2S_3 and CuS monomer which confirms successful preparation. The synthesized CuS/In_2S_3 show similar peak shape as CuS and the two peaks at 52.5°, 59.1° negative shift compared to CuS. And the Raman peak of CuS/In_2S_3 composites is positive shifted compared to CuS and negative shifted compared to In_2S_3 (Fig. 2c). The shift of XRD and Raman characteristic peaks indicates there is strong interaction between In_2S_3 and CuS.

As shown in Fig. S4, In_2S_3 and CuS was consisted of In/Cu, S, O and C. The XPS survey spectra prove the high purity of the photocatalysts. The two peaks of In 3*d* for In_2S_3 in Fig. 2d were indexed to 452.1 (In $3d_{3/2}$) and 444.5 eV (In $3d_{5/2}$), respectively and the two peaks of Cu 2*p* for CuS in Fig. 2e were corresponded to 951.6 (Cu $2p_{1/2}$) and 931.7 eV (Cu $2p_{3/2}$), respectively. The peaks of S 2*p* at 161.05 and 161.88 eV correspond to S-S. The banding energy centered at 162.45 and 163.03 eV are corresponded to S $2p_{3/2}$ and S $2p_{1/2}$ (Fig. 2f). When the CuS/In_2S_3 heterojunction is formed, the In 3*d* and S 2*p* of CuS/In_2S_3-4 show positive shift compared to the pristine In_2S_3, suggesting the loss of electrons from In_2S_3. On the contrary, the Cu 2*p* and S 2*p* orbitals of CuS/In_2S_3-4 show negative shift compared to CuS, proving the accumulation of the electrons from CuS.

As shown in Fig. 2g, the absorption band edge of In_2S_3 is at 600 nm. The CuS/In_2S_3 composite have broader absorption ability compared with the pristine In_2S_3. So it is possible to achieve improved photocatalytic performance. The band gap (E_g) of In_2S_3 and CuS are 1.79 and 1.72 eV, respectively (Fig. 2h). As shown in UPS spectra (Fig. 2i-k), the cutoff energies (E_{cutoff}) of In_2S_3, CuS and CuS/In_2S_3 were 16.30, 15.75 and 15.81 eV, respectively. The onset energies (E_{onset}) of In_2S_3 and CuS were 0.15 and 0.34 eV, respectively. The E_{VB} of In_2S_3 and CuS can be calculated by the formula: E_{VB} (vs. vacuum) = hν - (E_{cutoff} - E_{onset}), E_{VB} (vs. RHE) = E_{VB} (vs. vacuum) - 4.44 eV, where hν is 21.22 eV [37]. So, the E_{VB} of In_2S_3 and CuS are 0.63 and 1.37 eV, respectively. According to $E_{CB} = E_{VB}$ - Eg, the CBs of In_2S_3 and CuS are −1.23 and −0.35 V, respectively. The band structure of In_2S_3 and CuS is illustrated in Fig. 2l. And the work functions (Φ) of In_2S_3 and CuS are obtained by the formula: $\Phi = 21.22 - E_{cutoff}$ [38]. Therefore, the work functions of In_2S_3, CuS and CuS/In_2S_3 are 4.92, 5.47 and 5.41 eV, respectively. Thus, a compact interface is formed when In_2S_3 and CuS contact, the free electrons in In_2S_3 with a high E_F (-4.92 eV) would spontaneously diffuse to CuS with a low E_F (-5.47 eV) to equilibrate the E_F of two components [39]. The drifting of free electrons from In_2S_3 to CuS renders the charge redistribution at the interface between In_2S_3 to CuS, in which the interface near In_2S_3 side forms an electron depletion layer with positive charge, while an electron accumulation layer with negative charge appears near CuS side. As a result, this non-uniform interfacial charge distribution results in the formation of internal electric field pointing from In_2S_3 to CuS, which is consistent with the XPS results [40]. Based on the above results and analyses, a charge transfer mechanism of Z-scheme junction between In_2S_3 and CuS is depicted (Fig. 2m).

The atomic force microscope (AFM) equipped with Kelvin Probe Force Microscope (KPFM) has been done to further verify the existence of the internal electric field in CuS/In_2S_3. There was no significant change in the AFM images before and after visible-light irradiation (Fig. 3a, c), indicating that visible light had no effect on the morphology of CuS/In_2S_3. However, the surface potential diagrams of CuS/In_2S_3 in the dark and under light illumination were different (Fig. 3e). The average value of the surface potential along the blue line AB under dark

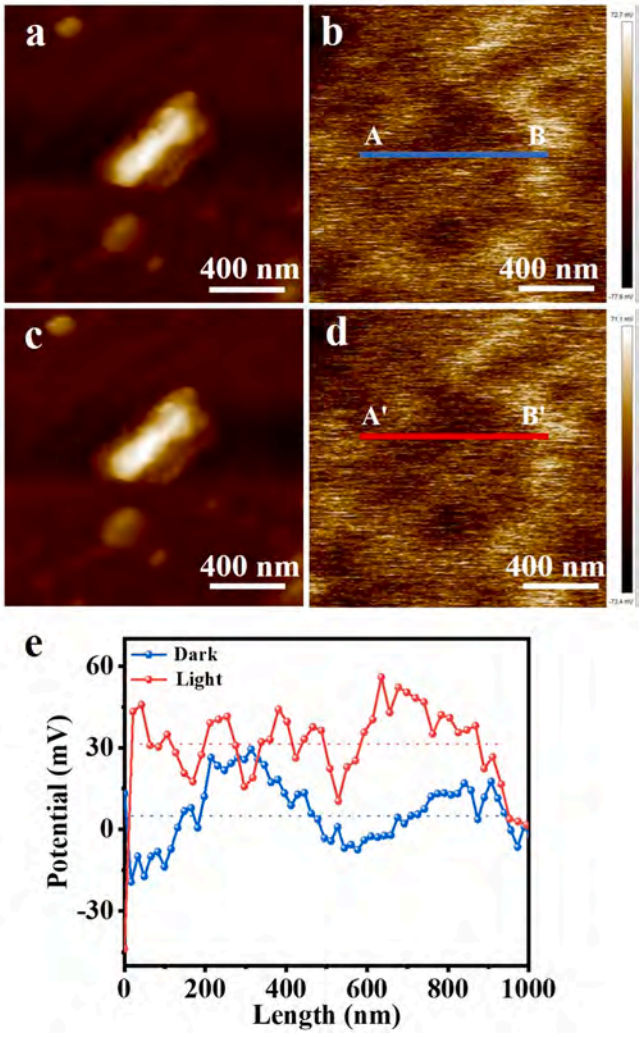

Fig. 3. AFM topographic images (a) in dark and (b) under light; KPFM images (c) in dark and (d) under light; (e) surface potential analysis along the blue line in (c) and along the red line in (d) for CuS/In_2S_3.

conditions was 4.8 mV, and the average value of the surface potential along the red line A'B' under light was 31.2 mV. The difference between the average surface potential under dark and light was about 26.4 mV. Due to the photoresponse of CuS/In_2S_3, the surface potential changes and the internal electric field were generated, which provided the driving force for the spatial separation of photogenerated electrons and holes [41,42].

3.2. Enhancement of photocatalytic MBT degradation activity

The photocatalytic properties of the materials were evaluated by testing the ability to degrade MBT under visible light irradiation. The degradation ability of pure In_2S_3, CuS and CuS/In_2S_3 was detected by the MBT degradation experiments in light condition. As shown in Fig. 4a-b, the self-degradation of MBT is negligible. Furthermore, the photocatalytic efficiency of pure In_2S_3, CuS and their physical mix is poor which only removed 12 %, 14 % and 17 % of MBT after light exposure for 90 min, respectively. In comparison, CuS/In_2S_3 have better photocatalytic performance. After only 1.5 h of light, CuS/In_2S_3-4 removes about 90 % of MBT. The pseudo-first-order reaction rate constant *k* for In_2S_3, CuS, CuS/In_2S_3-2, CuS/In_2S_3-4, CuS/In_2S_3-6 and CuS/In_2S_3-8 are 0.0012, 9.24×10^{-4}, 0.0092, 0.029, 0.026, and 0.019 min^{-1}, respectively (Fig. 4c). So, the degradation rate of MBT by CuS/In_2S_3-4 is most excellent. To be specific, the rates are

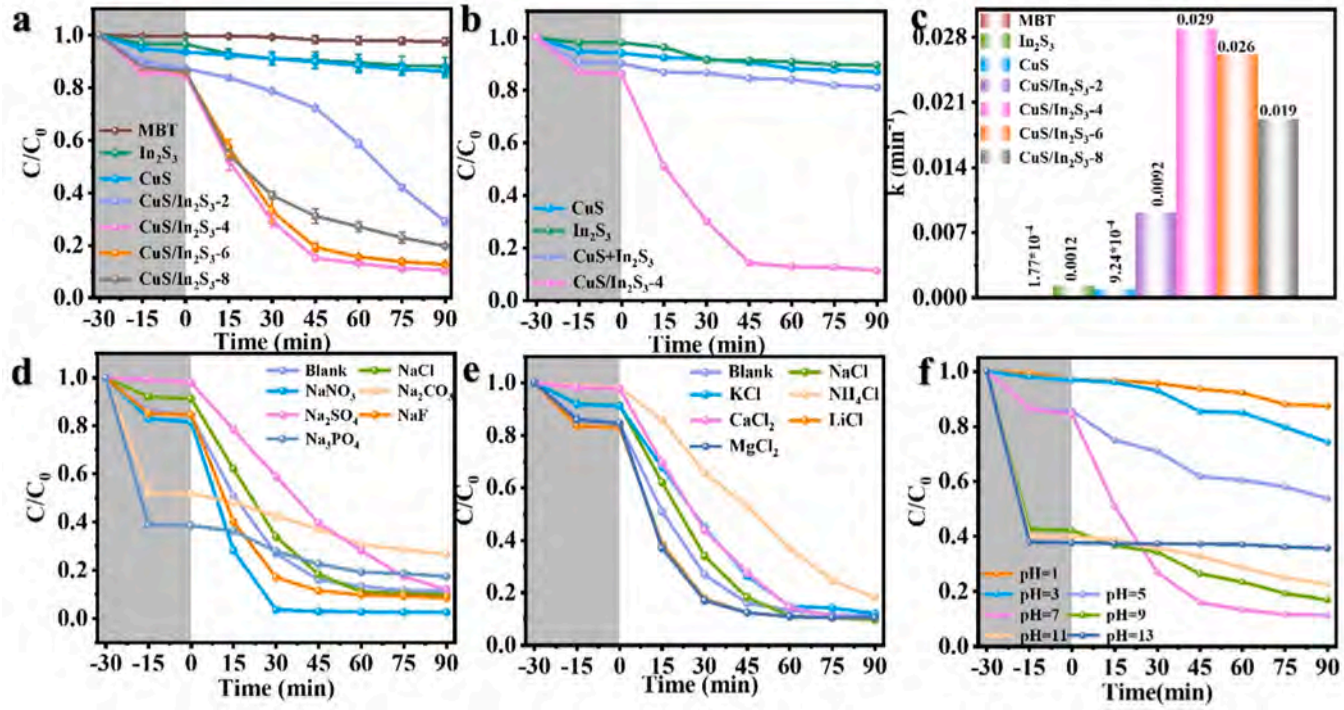

Fig. 4. (a, b) Photocatalytic properties for degradation of MBT under visible light irradiation; (c) reaction kinetics for degradation of MBT; Interference experiments for (d) positive ions, (e) negative ions, and (f) pH for MBT degradation in the presence of CuS/In_2S_3-4.

approximately 21.7 and 28.1 times faster than those of In_2S_3 and CuS, respectively. In addition, the performance of the CuS/ In_2S_3-4 composite material is much higher than that of the physical mixture of In_2S_3 and CuS, which indicates that the construction of the Z-scheme heterojunction of the CuS/In_2S_3-4 composite material plays a key role in the significant improvement of the photocatalytic performance.

As shown in Fig. 4d-e, in order to research the effect of cations, 1 mmol/L NH_4Cl, $MgCl_2$, NaCl, LiCl, KCl and $CaCl_2$ were introduced. In addition, the effect of anions was evaluated with NaCl, $NaNO_3$, Na_2SO_4, NaF, Na_3PO_4, and Na_2CO_3. These ions do not restrain the photocatalytic performance of CuS/In_2S_3 except NH_4Cl, Na_3PO_4 and Na_2CO_3. To assess the influence of pH, changed the pH from 1 to 13 with 2 M HNO_3 or

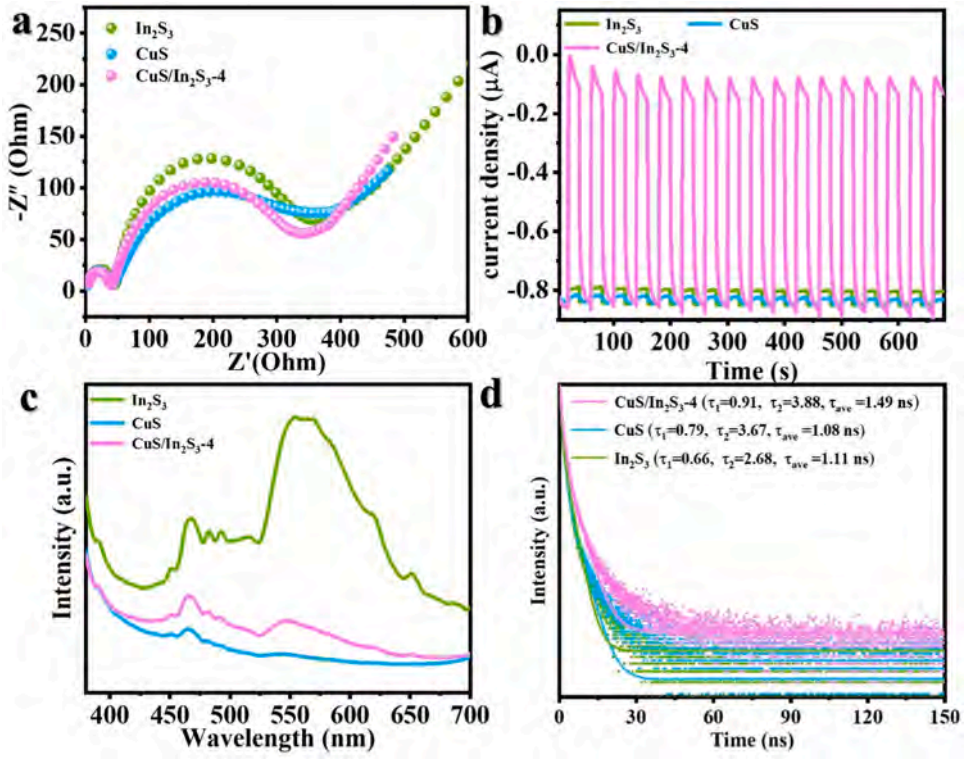

Fig. 5. (a) EIS spectra, (b) photocurrent curves, (c) PL spectra and (d) time-resolved fluorescence spectroscopy of In_2S_3, CuS and CuS/In_2S_3-4.

NaOH. As shown in Fig. 4f, the degradation efficiency of MBT decreases under both acidic and alkaline conditions. The pH value can affect both the surface properties of the photocatalysts and the chemical morphology of the substrates. In_2S_3 has amphoteric character and mercaptan (MBT) can be acid-base balanced. Consequently, the adsorption of the substrates may be affected to influence the degradation. The stability of CuS/In_2S_3-4 is assessed by cycling. And no significant deactivation was found in the degradation process of MBT even after five recycles proving the CuS/In_2S_3-4 has performance stability (Fig. S5). The CuS/In_2S_3-4 after cycling was measured by XRD (Fig. S6), SEM (Fig. S7), and TEM (Fig. S8). The results showed that the structure is largely the same and the morphology is the same to those before the cycle, corroborating its good stability.

Electrochemical impedance spectroscopy (EIS) was used to detect the resistance during charge transfer (Fig. 5a) [43–45]. The size of resistance can be determined based on the diameter of the Nyquist plot, and the smaller diameter means the lower resistance [46–48]. The Nyquist diameter of CuS/In_2S_3-4 is indeed smaller than those of the other materials. The results reveal that the construction of the heterojunction of CuS/In_2S_3 can reduce impedance and facilitate the charge transfer. As shown in Fig. 5b, for the photocurrent intensity, the CuS/In_2S_3-4 has the maximum photocurrent intensity. The photocurrents of pure In_2S_3 and CuS are smaller than those of other materials, certificating that CuS/In_2S_3 has the ability of quick photo-generated electrons separation and transport. In addition, the photocurrent intensity of the CuS/In_2S_3 composite material is also much higher than that of the sample of physical mixture of CuS and In_2S_3. This is mainly attributed to the Z-type electron migration mechanism induced by the built-in electric field between the CuS/In_2S_3 composite materials, which can significantly improve the separation efficiency of photogenerated carriers, while simple physical mixing has no the built-in electric field effect. Further steady-state photoluminescence (PL) spectra (Fig. 5c) show that CuS has the lowest intensity, which may be attributed to the fact that it produces fewer photogenerated electrons. Compared with In_2S_3, the PL intensity of CuS/In_2S_3-4 is significantly reduced. Time-resolved fluorescence spectroscopy (TRPL) was performed in Fig. 5d. The CuS/In_2S_3-4 exhibited a prolonged lifetime with a value of 1.49 ns, which is longer than that of In_2S_3 (1.11 ns) and CuS (1.08 ns). The above results show that the construction of CuS/In_2S_3-4 composite materials can effectively reduce the recombination probability of photogenerated carriers. And the carrier lifetimes was prolonged confirming the formation of Z-scheme heterojunctions.

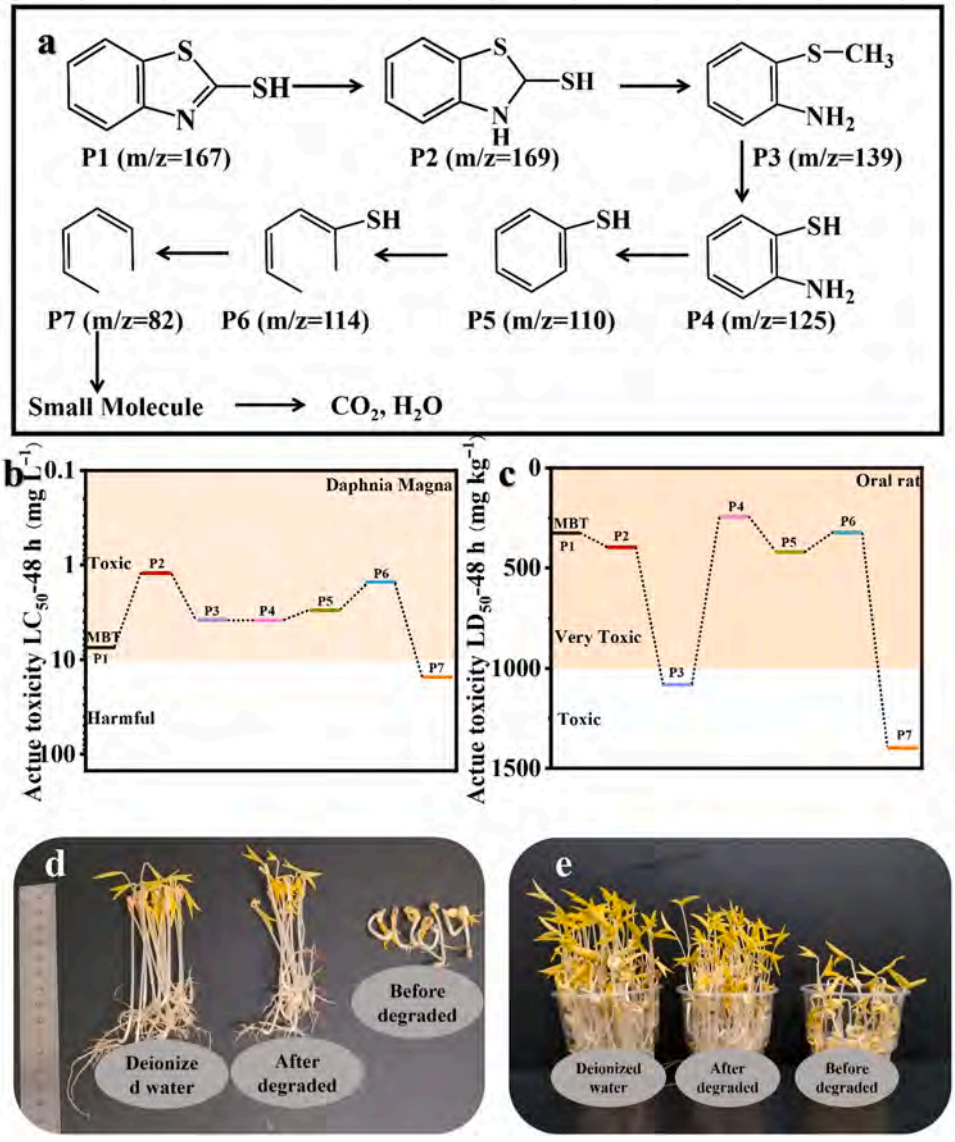

Fig. 6. (a) Possible degradation routes of MBT in CuS/In_2S_3-4; Daphnia magna LC_{50} (48 h) (b), Oral rat LD_{50} (48 h) (c) for degradation intermediates and MBT; (d, e) growing situation of mung bean seeds in deionized water as well as solution before and after photocatalytic degradation.

Mineralization of organic pollutants by CuS/In_2S_3-4 is assessed by TOC analysis during degradation (Fig. S9 and Table S1). The TOC removal efficiency of CuS/In_2S_3-4 is 39.87 %. To research the degradation mechanism of MBT, the products generated in the process of photocatalysis were detected by MS. The mass spectra of the solutions at different points in time is shown in Fig. S10, and it can be seen that many micromolecules were taken shape in the process of degradation. Based on the results, the degradation route of MBT is hypothesized [49–51]. As shown in Fig. 6a, the first step is to adsorb the MBT molecule on the surface of catalysts. MBT ($m/z = 167$) participated in the addition reaction to generate P2 ($m/z = 171$), and yielding P3 ($m/z = 139$) via dropping the -SH, followed by losing -CH_3 and -NH_2 to get P4 ($m/z = 125$) and P5 ($m/z = 110$), respectively. Wiping off the -SH and additive reaction leads to the P6 ($m/z = 114$) and P7 ($m/z = 82$). In the end, these smaller molecules were gradually disintegrated into CO_2 and H_2O. As shown in Fig. 6b-c, the toxicity of MBT and intermediate products were evaluated by Toxicity Estimation Software (T.E.S.T.). The Daphnia magna LC_{50} (48 h) was 15.05 mg/L for MBT, the values for the intermediates are lower than that of MBT. And the Oral rat LD_{50} (48 h) was 325.15 mg/kg for MBT, the values for P4 and P6 are lower than that of MBT. This suggests that more toxic molecules may be formed during the degradation process. But by observing the growth of mung beans, the toxicity of the solution after degradation is lower (Fig. 6d-e). The bud length watered with deionized water, degraded MBT solution (1 mg·L^{-1}) and undegraded MBT solution (10 mg·L^{-1}) was about 11, 10 and 2 cm, respectively. This further proof that photocatalytic reactions can effectively decompose organic pollutants.

The main active species in photocatalysis were studied through free radical trapping experiments and ESR [52,53]. As shown in Fig. 7a-b, the quenching of the hole (h^+), superoxide radical ($\cdot O_2^-$), hydroxyl radical (•OH) and singlet oxygen ($^1O_2$) was caused by the adding of Ammonium oxalate (AO), Ar, tert-butanol (TBA) and tryptophan (Trp), respectively. The introduction of AO and Ar inhibited the photocatalytic activity of CuS/In_2S_3-4. While the incorporation of TBA and Trp had no significant effect on the photocatalytic efficiency of CuS/In_2S_3-4 because the VBs position of CuS and In_2S_3 are both more negative than that of E^0(•OH/OH^-) (2.38 eV vs NHE). The results prove that h^+ and $\cdot O_2^-$ are the main active substances. ESR is carried out to further certificate the presence of h^+ and $\cdot O_2^-$. As a typical spin-labeled molecule, rhythms containing unpaired electrons exhibit a triplet ESR signal with an intensity ratio of 1:1:1 in the dark but under visible light irradiation, the signal strength is reduced due to the formation of TEMPOH. TEMPO on CuS/In_2S_3-4 is consumed faster within 10 min, indicating that CuS/In_2S_3-4 generates the biggest number of photo-generated electrons and holes under simulated sunlight (Fig. 7c). In the CuS/In_2S_3 system, no signal peaks for DMPO-·O_2^- (Fig. 7d) and DMPO-·OH (Fig. 7e) in dark. However, after the light, both pure In_2S_3 and CuS/In_2S_3-4 produce DMPO-·O_2^- signal, and the signal from CuS/In_2S_3-4 is stronger than that of In_2S_3. However, the signal of DMPO-·OH cannot be seen from the three photocatalysts. According to the above results, the possible reaction mechanism is raised. As shown in Fig. 7f, electrons in VBs of CuS and In_2S_3 are shifted to CBs under visible light illumination. Due to the construction of the internal electric field between CuS and In_2S_3, electrons in CB of CuS combine with the holes in VB of In_2S_3 and the holes in VB of CuS and the electrons in CB of In_2S_3 are reserved. And electrons in In_2S_3 reduce O_2 to $\cdot O_2^-$ ($E^0O_2/\cdot O^{2-} = -0.046$ eV vs NHE) and holes in CuS directly oxidize the MBT molecules. Finally, $\cdot O_2^-$ and h^+ oxidize the molecules to CO_2 and H_2O. Therefore, the CuS/In_2S_3-4 Z-scheme heterojunction effectively segregates the photo-induced carriers, and also reserves redox ability of the pristine photocatalysts.

4. Conclusion

In conclusion, the CuS/In_2S_3 Z-scheme heterojunction is devised and constructed successfully. The CuS nanosheets grow evenly on the surface of the In_2S_3 hollow tubular. UPS, free radicals trapping experiments and ESR prove that the photogenerated electrons are transported from CuS to In_2S_3 through Z-Scheme mechanism. The construction of Z-scheme

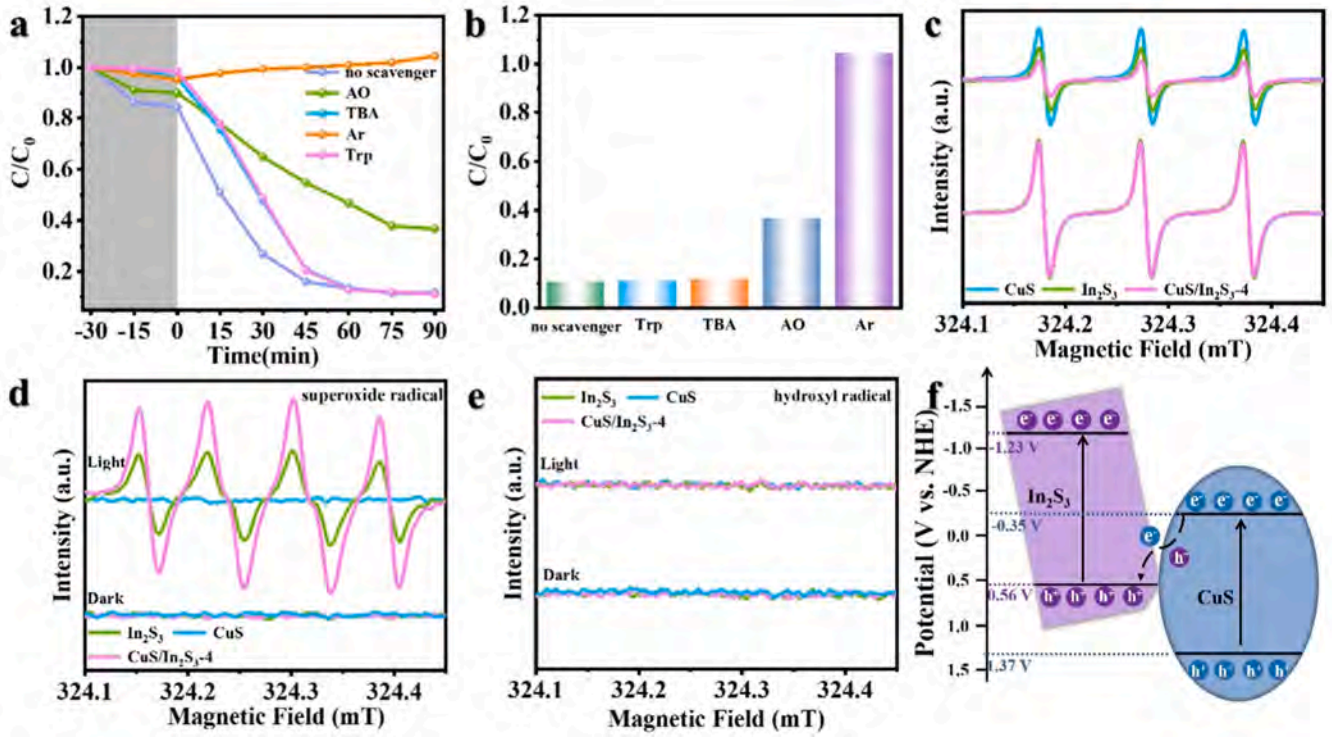

Fig. 7. (a, b) Comparison of the photocatalytic activities of CuS/In_2S_3-4 for the degradation of MBT with or without adding TBA, AO, Trp, and Ar under visible light irradiation; ESR spectra of (c) holes, (d) DMPO-·O_2^-, (e) DMPO-·OH of In_2S_3, CuS and CuS/In_2S_3-4; (f) Mechanism and role of CuS/In_2S_3-4 in photocatalytic degradation.

heterojunction not only effectively segregates the photo-generated carriers, but also reserves the redox capacity of the pristine photocatalysts. Compared to pure CuS and In_2S_3, CuS/In_2S_3-4 represents better photocatalytic performance in the degradation of MBT. And the cultivation of bean sprouts showed that the toxicity of the solution after degradation was very low. In the photocatalytic degradation of MBT, $\cdot O_2^-$ and h^+ are the main active substances. The constructing of Z-scheme heterojunction has important implications to improve the activity of the photocatalysts.

CRediT authorship contribution statement

Liu Gaopeng: Writing – review & editing, Funding acquisition, Formal analysis. **Yan Xingwang:** Writing – review & editing, Formal analysis, Data curation. **Zhao Junze:** Writing – review & editing, Methodology, Formal analysis, Data curation. **Wang Bin:** Writing – review & editing, Writing – original draft, Funding acquisition, Formal analysis, Data curation, Conceptualization. **Yang Tingting:** Writing – review & editing, Writing – original draft, Formal analysis, Data curation, Conceptualization. **Chu Paul K.:** Writing – review & editing, Resources, Funding acquisition. **Ji Mengxia:** Writing – review & editing, Formal analysis, Conceptualization. **Li Huaming:** Writing – review & editing, Supervision, Funding acquisition, Formal analysis, Conceptualization. **Xia Jiexiang:** Writing – review & editing, Supervision, Funding acquisition, Conceptualization.

Declaration of Competing Interest

The authors declare that they have no conflicts of interest.

Acknowledgements

This work was financially supported by the National Natural Science Foundation of China (Nos. 22108106, 22108108), City University of Hong Kong Donation Research Grant (DON-RMG No. 9229021) and Key Laboratory of Electrochemical Energy Storage and Energy Conversion of Hainan Province (KFKT2024005).

Appendix A. Supporting information

Supplementary data associated with this article can be found in the online version at doi:10.1016/j.jece.2025.115542.

Data availability

Data will be made available on request.

References

[1] Q.H. Zhu, Q. Xu, M.M. Du, X.F. Zeng, G.F. Zhong, B.C. Qiu, J.L. Zhang, Zhang, Recent progress of metal sulfide photocatalysts for solar energy conversion, Adv. Mater. 34 (2022), https://doi.org/10.1002/adma.202202929.

[2] S. Yu, X.B. Fan, X. Wang, J.G. Li, Q. Zhang, A.D. Xia, S.Q. Wei, L.Z. Wu, Y. Zhou, G. R. Patzke, Efficient photocatalytic hydrogen evolution with ligand engineered all-inorganic InP and InP/ZnS colloidal quantum dots, Nat. Commun. 9 (2018), https://doi.org/10.1038/s41467-018-06294-y.

[3] B. Wang, W. Zhang, G.P. Liu, H.L. Chen, Y.X. Weng, H.M. Li, P.K. Chu, J.X. Xia, Excited electron-Rich $Bi^{(3-x)+}$ sites: a quantum well-like structure for highly promoted selective photocatalytic co2 reduction performance, Adv. Funct. Mater. 32 (2022), https://doi.org/10.1002/adfm.202202885.

[4] R. Ji, J.D. Liu, T.Y. Zhang, Y. Peng, Y.Y. Li, D.Y. Chen, Q.F. Xu, J.M. Lu, Construction of a ternary Z-scheme In_2S_3@Au@P3HT photocatalyst for the degradation of phenolic pollutants under visible light, Sep. Purif. Technol. 272 (2021), https://doi.org/10.1016/j.seppur.2021.118787.

[5] B. Wang, H.L. Chen, W. Zhang, H.Y. Liu, Z.K. Zheng, F.C. Huang, J.Y. Liu, G.P. Liu, X.W. Yan, Y.X. Weng, H.M. Li, Y.B. She, P.K. Chu, J.X. Xia, Semimetallic bismuthene with edge-rich dangling bonds: broad-spectrum-driven and edge-confined electron enhancement boosting CO_2 hydrogenation reduction, Adv. Mater. 36 (2024), https://doi.org/10.1002/adma.202312676.

[6] S. Lee, P. Seraffni, S. Masi, A.F. Gualdrón-Reyes, C.A. Mesa, J. Rodríguez-Pereira, S. Giménez, H.J. Lee, I. Mora-Seró, A perovskite photovoltaic mini-module-$CsPbBr_3$ photoelectrochemical cell tandem device for solar-driven degradation of organic compounds, ACS Energy Lett. 8 (2023) 4488–4495. ⟨http://pubs.acs.org/journal/aelccp⟩.

[7] C. Yang, X.F. Hu, Y. Huang, B.Y. Liu, J.H. Yang, Pyrrole nitrogen coordinated Fe on carbon nitride mediated singlet oxygen formation for efficient degradation of 2-mercaptobenzothiazole, J. Environ. Chem. Eng. 11 (2023), https://doi.org/10.1016/j.jece.2023.109694.

[8] Y.S. Zeng, Q. Yin, Z. Liu, H. Dong, Attapulgite-interpenetrated g-C_3N_4/Bi_2WO_6 quantum-dots Z-scheme heterojunction for 2-mercaptobenzothiazole degradation with mechanism insight, Chem. Eng. J. 435 (2022), https://doi.org/10.1016/j.cej.2022.134918.

[9] Z.R. Salah, R. Salah, M.A. Malouki, B. Khennaoui, J.A. Santaballa, M. Canle, Simulated sunlight photodegradation of 2-mercaptobenzothiazole by heterogeneous photo-Fenton using a natural clay powder, J. Environ. Chem. Eng. 6 (2018) 1783–1793, https://doi.org/10.1016/j.jece.2018.02.011.

[10] J. Kim, J. Lee, S. Kim, T. Kim, K.M. Lee, D. Lee, J. Cho, J.Y. Kim, Y.W. Jeong, H. J. Park, J.C. Lee, C. Lee, Virucidal activity of Cu-doped TiO_2 nanoparticles under visible light illumination: effect of Cu oxidation state, J. Hazard. Mater. 465 (2024), https://doi.org/10.1016/j.jhazmat.2024.133525.

[11] X.D. Li, Y.F. Sun, J.Q. Xu, Y.J. Shao, J. Wu, X.L. Xu, Y. Pan, H.X. Ju, J.F. Zhu, Y. Xie, Selective visible-light-driven photocatalytic CO_2 reduction to CH_4 mediated by atomically thin $CuIn_5S_8$ layers, Nat. Energy 4 (2019) 690–699, https://doi.org/10.1038/s41560-019-0431-1.

[12] B. Wang, J.Z. Zhao, H.L. Chen, Y.X. Weng, H. Tang, Z.R. Chen, W.S. Zhu, J.X. Xia, H.M. Li, Unique Z-scheme carbonized polymer dots/$Bi_4O_5Br_2$ hybrids for efficiently boosting photocatalytic CO_2 reduction, Appl. Catal. B Environ. 293 (2021), https://doi.org/10.1016/j.apcatb.2021.120182.

[13] H.J. Wang, X. Li, X.X. Zhao, C.Y. Li, X.H. Song, P. Zhang, P.W. Huo, X. Li, A review on heterogeneous photocatalysis for environmental remediation: from semiconductors to modification strategies, Chin. J. Catal. 43 (2022) 178–214. ⟨http://www.sciencedirect.com/journal/chinese-journal-of-catalysis⟩.

[14] S. Jadoun, J. Yáñez, H.D. Mansilla, U. Riaz, N.P.S. Chauhan, Conducting polymers/zinc oxide-based photocatalysts for environmental remediation: a review, Environ. Chem. Lett. 20 (2022) 2063–2083, https://doi.org/10.1007/s10311-022-01398-w.

[15] J.Z. Zhao, M.X. Ji, H.L. Chen, Y.X. Weng, J. Zhong, Y.J. Li, S.Y. Wang, Z.R. Chen, J. X. Xia, H.M. Li, Interfacial chemical bond modulated $Bi_{19}S_{27}Br_3$/g-C_3N_4 Z-scheme heterojunction for enhanced photocatalytic CO_2 conversion, Appl. Catal. B Environ. 307 (2022), https://doi.org/10.1016/j.apcatb.2022.121162.

[16] X.F. Li, X.L. Shen, Y.L. Qiu, Z.L. Zhu, H. Zhang, D.Q. Yin, Fe_3O_4 quantum dots mediated P-g-C_3N_4/BiOI as an efficient and recyclable Z-scheme photo-Fenton catalyst for tetracycline degradation and bacterial inactivation, J. Hazard. Mater. 456 (2023), https://doi.org/10.1016/j.jhazmat.2023.131677.

[17] J.T. Dong, S.N. Ji, Y. Zhang, M.X. Ji, B. Wang, Y.J. Li, Z.G. Chen, J.X. Xia, H.M. Li, Construction of Z-Scheme MnO_2/BiOBr Heterojunction for Photocatalytic Ciprofloxacin Removal and CO_2 Reduction, Acta Phys. -Chim. Sin. 39 (2023). ⟨https://www.whxb.pku.edu.cn/EN/Y2023/V39/I11/2212011⟩.

[18] B.Q. Xia, B.W. He, J.J. Zhang, L.Q. Li, Y.H. Zhang, J.G. Yu, J.R. Ran, S.Z. Qiao, TiO_2/$FePS_3$ S-scheme heterojunction for greatly raised photocatalytic hydrogen evolution, Adv. Energy Mater. 12 (2022), https://doi.org/10.1002/aenm.202201449.

[19] S.B. Wang, B.Y. Guan, X.W. Lou, Construction of $ZnIn_2S_4$-In_2O_3 hierarchical tubular heterostructures for efficient CO_2 photoreduction, J. Am. Chem. Soc. 140 (2018) 5037–5040, https://doi.org/10.1021/jacs.8b02200.

[20] X. Xin, Y.K. Li, Y.Z. Zhang, Y.J. Wang, X. Chi, Y.P. Wei, C.Z. Diao, J. Su, R.L. Wang, P. Guo, J.K. Yu, J. Zhang, A.J. Sobrido, M.M. Titirici, X.H. Li, Large electronegativity differences between adjacent atomic sites activate and stabilize $ZnIn_2S_4$ for efficient photocatalytic overall water splitting, Nat. Commun. 15 (2024), https://doi.org/10.1038/s41467-024-44725-1.

[21] J.Q. Li, Y.Q. Mei, S.C. Ma, Q.F. Yang, B.J. Jiang, B.F. Xin, T.J. Yao, J. Wu, Internal-electric-field induced high efficient type-I heterojunction in photocatalysis-self-Fenton reaction: Enhanced H_2O_2 yield, utilization efficiency and degradation performance, J. Colloid Interface Sci. 608 (2022) 2075–2087, https://doi.org/10.1016/j.jcis.2021.10.119.

[22] X.Y. Meng, S.Y. Wang, C.C. Zhang, C.Z. Dong, R. Li, B.N. Li, Q. Wang, Y. Ding, Boosting hydrogen evolution performance of a CdS-based photocatalyst: in situ transition from type I to type II heterojunction during photocatalysis, ACS Catal. 12 (2022) 10115–10126, https://doi.org/10.1021/acscatal.2c01877.

[23] X.W. Yan, B. Wang, J.Z. Zhao, G.P. Liu, M.X. Ji, X.L. Zhang, P.K. Chu, H.M. Li, J. X. Xia, Hierarchical columnar $ZnIn_2S_4$/$BiVO_4$ Z-scheme heterojunctions with carrier highway boost photocatalytic mineralization of antibiotics, Chem. Eng. J. 452 (2023), https://doi.org/10.1016/j.cej.2022.139271.

[24] Y. Wang, J.X. Xu, J. Wan, J. Wang, L. Wang, A tube-like dual Z-scheme indium oxide@indium phosphide/cuprous oxide photocatalyst based on metal-organic framework for efficient CO_2 reduction with water, J. Colloid Interface Sci. 616 (2022) 532–539, https://doi.org/10.1016/j.jcis.2022.02.101.

[25] X.W. Ruan, C.X. Huang, H. Cheng, Z.Q. Zhang, Y. Cui, Z.Y. Li, T.F. Xie, K.K. Ba, H. Y. Zhang, L. Zhang, X. Zhao, J. Leng, S.Y. Jin, W. Zhang, W.T. Zheng, S.K.R. Ravi, Z.F. Jiang, X.Q. Cui, J.G. Yu, A twin S-scheme artiffcial photosynthetic system with self-assembled heterojunctions yields superior photocatalytic hydrogen evolution rate, Adv. Mater. 35 (2023), https://doi.org/10.1002/adma.202209141.

[26] C. Cheng, J.J. Zhang, B.C. Zhu, G.J. Liang, L.Y. Zhang, J.G. Yu, Verifying the charge-transfer mechanism in S-scheme heterojunctions using femtosecond transient absorption spectroscopy, Angew. Chem. Int. Ed. 62 (2023), https://doi.org/10.1002/anie.202218688.

[27] Y.H. Pi, S. Jin, X.Y. Li, S. Tu, Z. Li, J. Xiao, Encapsulated MWCNT@MOF-derived In_2S_3 tubular heterostructures for boosted visible-light-driven degradation of

tetracycline, Appl. Catal. B Environ. 256 (2019), https://doi.org/10.1016/j.apcatb.2019.117882.
[28] K. Yan, D.H. Wu, T. Wang, C. Chen, S.J. Liu, Y.G. Hu, C. Gao, H.Y. Chen, B.X. Li, Highly Selective Ethylene Production from Solar-Driven CO_2 Reduction on the Bi_2S_3@In_2S_3 Catalyst with In-S_V-Bi Active Sites, ACS Catal. 13 (2023), https://doi.org/10.1021/acscatal.2c05741.
[29] S.Q. Liu, W.L. Qi, S. Adimi, H.C. Guo, B. Weng, John Paul Attfield, Minghui Yang, Titanium nitride-supported platinum with metal-support interaction for boosting photocatalytic h2 evolution of indium sulfide, ACS Appl. Mater. Interfaces 13 (2021) 7238–7247, https://doi.org/10.1021/acsami.0c20919.
[30] Z.Y. He, Y. Wang, X.L. Dong, N. Zheng, H.C. Ma, X.F. Zhang, Indium sulfide nanotubes with sulfur vacancies as an efficient photocatalyst for nitrogen fixation, RSC Adv. 9 (2019), https://doi.org/10.1039/C9RA03507A.
[31] L.P. Chi, Z.Z. Niu, X.L. Zhang, P.P. Yang, J. Liao, F.Y. Gao, Z.Z. Wu, K.B. Tang, M. R. Gao, Stabilizing indium sulfide for CO_2 electroreduction to formate at high rate by zinc incorporation, Nat. Commun. 12 (2021), https://doi.org/10.1038/s41467-021-26124-y.
[32] J.B. Wang, Y.N. Wang, M.Y. Yu, G.J. Li, S.L. Zhang, Q. Zhong, Formation of flaky carbon nitride and beta-Indium sulfide heterojunction with efficient separation of charge carriers for enhanced photocatalytic carbon dioxide reduction, J. Colloid Interface Sci. 611 (2022) 71–81, https://doi.org/10.1016/j.jcis.2021.12.081.
[33] Z.B. Wu, X.Z. Yuan, G.M. Zeng, L.B. Jiang, H. Zhong, Y.C. Xie, H. Wang, X.H. Chen, H. Wang, Highly efficient photocatalytic activity and mechanism of Yb^{3+}/Tm^{3+} codoped In_2S_3 from ultraviolet to near infrared light towards chromium (VI) reduction and rhodamine B oxydative degradation, Appl. Catal. B Environ. 225 (2018) 8–21, https://doi.org/10.1016/j.apcatb.2017.11.040.
[34] V. Soni, P. Raizada, A. Kumar, V. Hasija, S. Singal, P. Singh, H.B. Ahmad, V. K. Thakur, V.H. Nguyen, Indium sulfde-based photocatalysts for hydrogen production and water cleaning: a review, Environ. Chem. Lett. 19 (2021) 1065–1095, https://doi.org/10.1007/s10311-020-01148-w.
[35] Y.Z. Zhang, N.X. Miao, X. Xin, Y.J. Wang, J.M. Zhu, P. Guo, J.J. Wang, J. Ana Sobrido, M.M. Titirici, X.H. Li, Boosting the photocatalytic performance via defect-dependent interfacial interactions from electrostatic adsorption to chemical bridging, Nano Energy 104 (2022), https://doi.org/10.1016/j.nanoen.2022.107865.
[36] S.B. Wang, B.Y. Guan, Y. Lu, X.W. Lou, Formation of hierarchical In_2S_3-$CdIn_2S_4$ heterostructured nanotubes for efficient and stable visible light CO_2 reduction, J. Am. Chem. Soc. 139 (2017) 17305–17308, https://doi.org/10.1021/jacs.7b10733.
[37] P.Y. Zhou, Y. Wang, X.R. Yan, Y. Gan, C.K. Xia, Y.G. Xu, M. Xie, Nitrogen-defect-modiffed g-C_3N_4/$BaFe_{12}O_{19}$ S-scheme heterojunction photocatalyst with enhanced advanced oxidation technology synergistic photothermal degradation ability of antibiotic: insights into performance, electron transfer pathways and toxicity, Appl. Catal. B Environ. 343 (2024), https://doi.org/10.1016/j.apcatb.2023.123485.
[38] M.L. Sheng, C. Gan, Y. Li, Z.J. Hu, Q. Zhou, L. Qin, J.M. Ren, H.Y. Jiang, Photocatalytic C-O activation and biomass derived polymer precursor production with CO_2 over redox centers spatially separated Sv-$ZnIn_2S_4$/$BiVO_4$, Appl. Catal. B Environ. 339 (2023), https://doi.org/10.1016/j.apcatb.2023.123138.
[39] B.W. He, P. Xiao, S.J. Wan, J.J. Zhang, T. Chen, L.Y. Zhang, J.G. Yu, Rapid charge transfer endowed by interfacial Ni-O bonding in S-scheme heterojunction for efficient photocatalytic H_2 and imine production, Angew. Chem. Int. Ed. 62 (2023), https://doi.org/10.1002/anie.202313172.
[40] Z.J. Zhu, H.W. Huang, L.Z. Liu, F. Chen, N. Tian, Y.H. Zhang, H. Yu, Chemically bonded α-Fe_2O_3/Bi_4MO_8Cl dot-on-plate Z-scheme junction with strong internal electric field for selective photooxidation of aromatic alcohols, Angew. Chem. Int. Ed. 61 (2022), https://doi.org/10.1002/anie.202203519.
[41] Z.Z. Chen, Y.J. Yan, P.N. Shan, A. Bian, W. Kong, A. Proskurin, L. Guo, Jianhua Hou, Zhuo Liu, Guangzhao Wang, Weilong Shi, Changyu Lu, Interfacial reconstruction of 2D/2D CuS/$ZnIn_2S_4$ through interface S-S bonds for boosted near-infrared driven photothermal-assisted photocatalytic hydrogen production, J. Alloy. Compd. 1009 (2024), https://doi.org/10.1016/j.jallcom.2024.176891.
[42] X.W. Xu, F. Deng, P.H. Shao, D.D. Dionysiou, X.B. Luo, X.B. Li, S.Q. Zhang, X. G. Liu, M. Liu, Internal electric ffeld driving separation and migration of charge carriers via Z-scheme path in $AgIn_5S_8$/ZnO heterojunction for efficient decontamination of pharmaceutical pollutants, Chem. Eng. J. 428 (2022), https://doi.org/10.1016/j.cej.2021.132096.
[43] X. Cheng, X.Y. Xiao, F. Wang, T. Lu, Y. Zhang, Heterojunctions Based on BiOBr Nanosheets Decorated on α-Bi_2O_3 for Photodegradation of Rhodamine B, ACS Appl. Nano Mater. 7 (2024) 4413–4422, https://doi.org/10.1021/acsanm.3c05957.
[44] J. Wang, T.L. Yang, R. He, K.H. Xue, R.R. Sun, W.L. Wang, J.T. Wang, T. Yang, Y. L. Wang, Silver-loaded In_2S_3-$CdIn_2S_4$@X(X=Ag, Ag_3PO_4, AgI) ternary heterostructure nanotubes treated by electron beam irradiation with enhanced photocatalytic activity, Sci. Total. Environ. 695 (2019), https://doi.org/10.1016/j.scitotenv.2019.133884.
[45] C. Wu, W.X. Huang, H.M. Liu, K.L. Lv, Q. Li, Insight into synergistic effect of Ti_3C_2 MXene and MoS_2 on anti-photocorrosion and photocatalytic of CdS for hydrogen production, Appl. Catal. B Environ. 330 (2023), https://doi.org/10.1016/j.apcatb.2023.122653.
[46] G.P. Liu, L. Wang, X. Chen, X.W. Zhu, B. Wang, X.Y. Xu, Z.R. Chen, W.S. Zhu, H. M. Li, J.X. Xia, Crafting of plasmonic Au nanoparticles coupled ultrathin BiOBr nanosheetsheterostructure: steering charge transfer for efficient CO_2 photoreduction, Green Chem. Eng. 3 (2022) 157–164, https://doi.org/10.1016/j.gce.2021.11.007.
[47] H.W. He, Z.L. Wang, K. Dai, S.W. Li, J.F. Zhang, LSPR-enhanced carbon-coated In_2O_3/$W_{18}O_{49}$ S-scheme heterojunction for efficient CO_2 photoreduction, Chin. J. Catal. 48 (2023) 267–278, https://doi.org/10.1016/S1872-2067(23)64420-1.
[48] G.P. Liu, L. Wang, B. Wang, X.W. Zhu, J.M. Yang, P.J. Liu, W.S. Zhu, Z.R. Chen, J. X. Xia, Synchronous activation of Ag nanoparticles and BiOBr for boosting solar-driven CO_2 reduction,, Chin. Chem. Lett. 34 (2023) 107962, https://doi.org/10.1016/j.cclet.2022.107962.
[49] Y.Y. Qin, H. Li, J. Lu, Y.C. Ding, C.C. Ma, X.L. Liu, Z. Liu, P.W. Huo, Y.S. Yan, Photocatalytic degradation of 2-Mercaptobenzothiazole by a novel Bi_2WO_6 nanocubes/$In(OH)_3$ photocatalyst: Synthesis process, degradation pathways, and an enhanced photocatalytic performance mechanism study, Appl. Surf. Sci. 481 (2019) 1313–1326, https://doi.org/10.1016/j.apsusc.2019.03.244.
[50] Z. Zhu, C.C. Ma, K.S. Yu, Z.Y. Lu, Z. Liu, P.W. Huo, T. Xu, Y.S. Yan, Synthesis Ce-doped biomass carbon-based g-C_3N_4 via plant growing guide and temperature-programmed technique for degrading 2-Mercaptobenzothiazole, Appl. Catal. B Environ. 268 (2020), https://doi.org/10.1016/j.apcatb.2019.118432.
[51] Z. Zhu, Y. Yu, H.J. Dong, Z. Liu, C.X. Li, P.W. Huo, Y.S. Yan, Intercalation effect of attapulgite in g-C_3N_4 modified with Fe_3O_4 quantum dots to enhance photocatalytic activity for removing 2-mercaptobenzothiazole under visible light, ACS Sustain. Chem. Eng. 5 (2017) 10614–10623, https://doi.org/10.1021/acssuschemeng.7b02595.
[52] C. Zhang, S.H. Tian, F.Z. Qin, Y.L. Yu, D.L. Huang, A.B. Duan, C.Y. Zhou, Y. Yang, W.J. Wang, Y. Zhou, H.Z. Luo, Catalyst-free activation of permanganate under visible light irradiation for sulfamethazine degradation: experiments and theoretical calculation, Water Res. 194 (2021), https://doi.org/10.1016/j.watres.2021.116915.
[53] F. Zhang, J.Y. Xin, X. Wu, J. Liu, L.Y. Niu, D. Wang, X.H. Li, C.L. Shao, X.W. Li, Y. C. Liu, Floating metal phthalocyanine@polyacrylonitrile nanofibers for peroxymonosulfate activation: synergistic photothermal effects and highly efficient flowing wastewater treatment, J. Hazard. Mater. 459 (2023), https://doi.org/10.1016/j.jhazmat.2023.132228.

Constructing highly effective CuS/In_2S_3 Z-scheme heterojunction with boosted charge transfer for enhanced photocatalytic performance

Tingting Yang [a], Bin Wang [a,b,*], Xingwang Yan [a], Gaopeng Liu [a], Junze Zhao [a], Mengxia Ji [a], Paul K. Chu [b], Jiexiang Xia [a,*], Huaming Li [a,*]

[a] *School of Chemistry and Chemical Engineering, Institute for Energy Research, Jiangsu University, 301 Xuefu Road, Zhenjiang 212013, China*

[b] *Department of Physics, Department of Materials Science and Engineering, and Department of Biomedical Engineering, City University of Hong Kong, Tat Chee Avenue, Kowloon, Hong Kong, China*

* Corresponding authors: wangbin@ujs.edu.cn (B. Wang); xjx@ujs.edu.cn (J. Xia); lhm@ujs.edu.cn (H. Li)

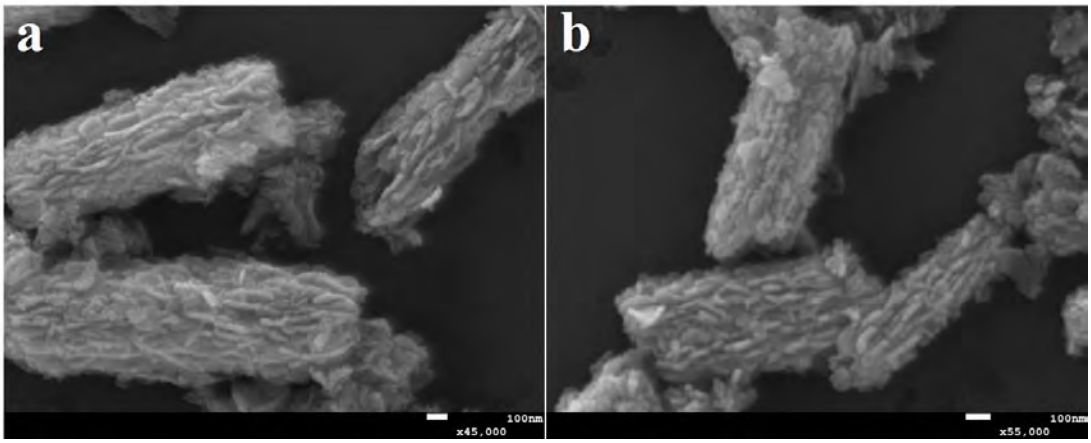

Fig. S1. SEM images of CuS/In_2S_3-4 with lower magnification.

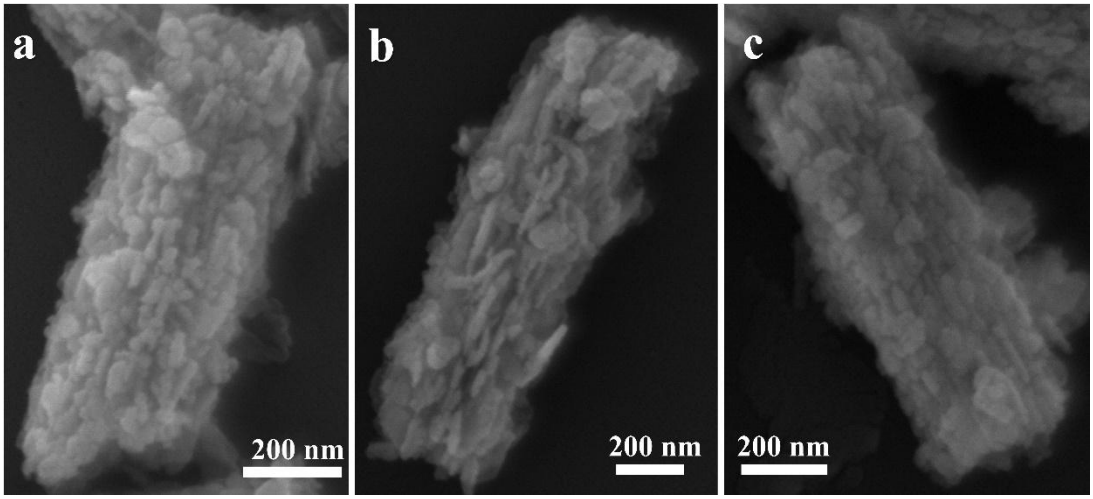

Fig. S2. SEM images of (a) CuS/In_2S_3-2, (b) CuS/In_2S_3-6 and (c) CuS/In_2S_3-8.

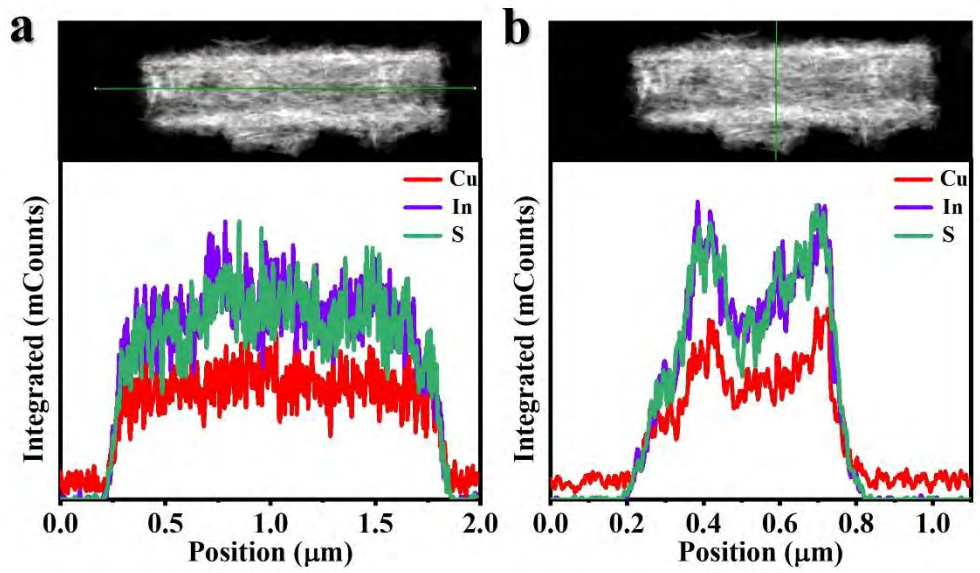

Fig. S3. Line scan spectra of CuS/In_2S_3-4.

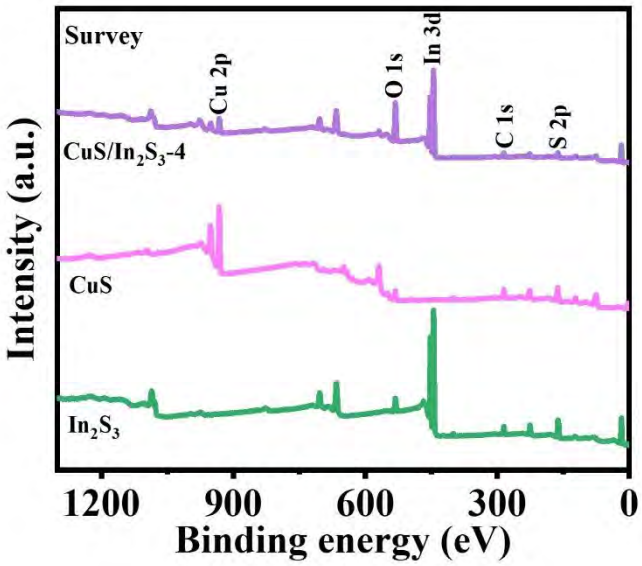

Fig. S4. XPS spectrum of CuS, In_2S_3 and CuS/In_2S_3-4.

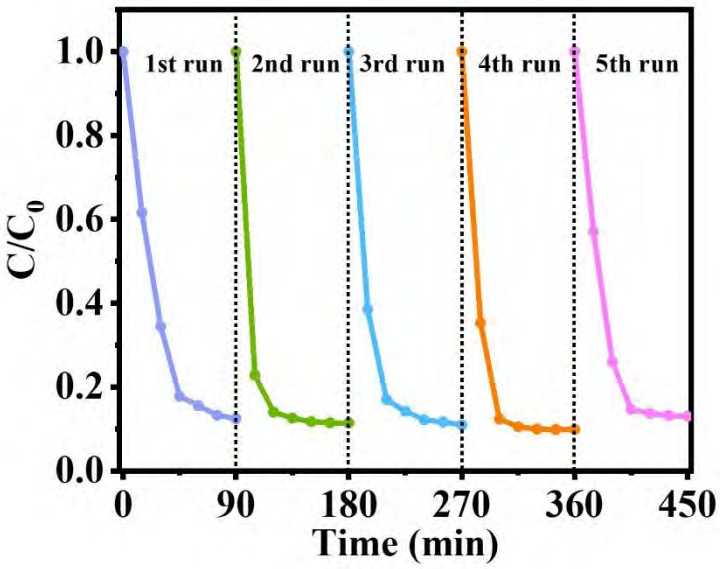

Fig. S5. Cycling experiments in the presence of CuS/In_2S_3-4.

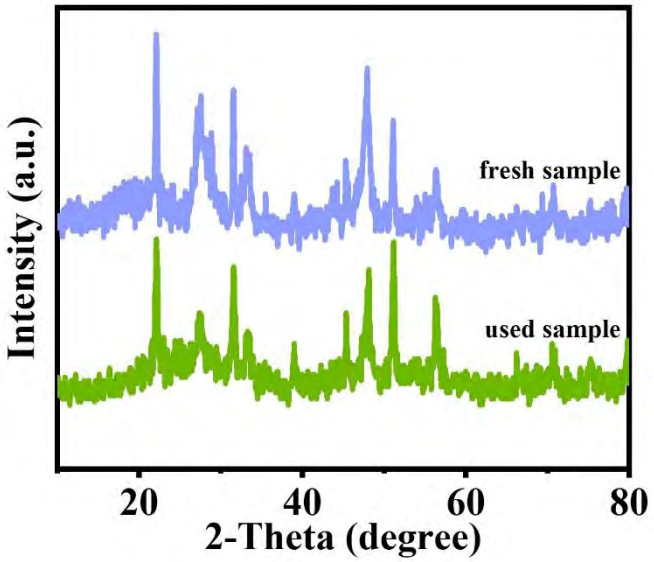

Fig. S6. XRD patterns of CuS/In_2S_3-4 before and after cycling.

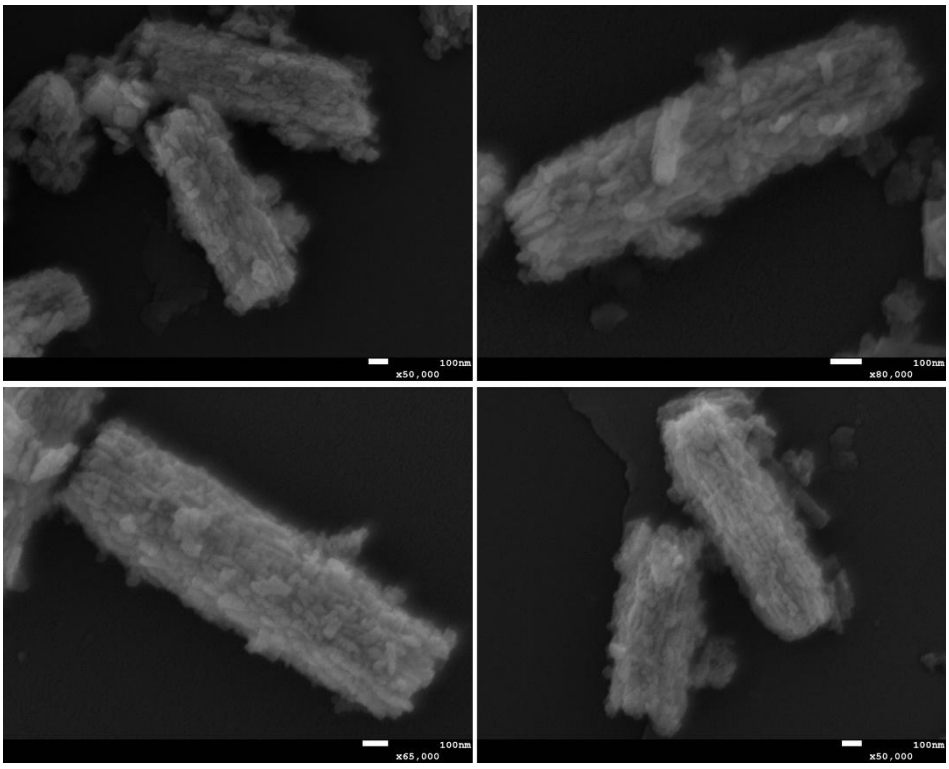

Fig. S7. SEM images of CuS/In_2S_3-4 after cycling.

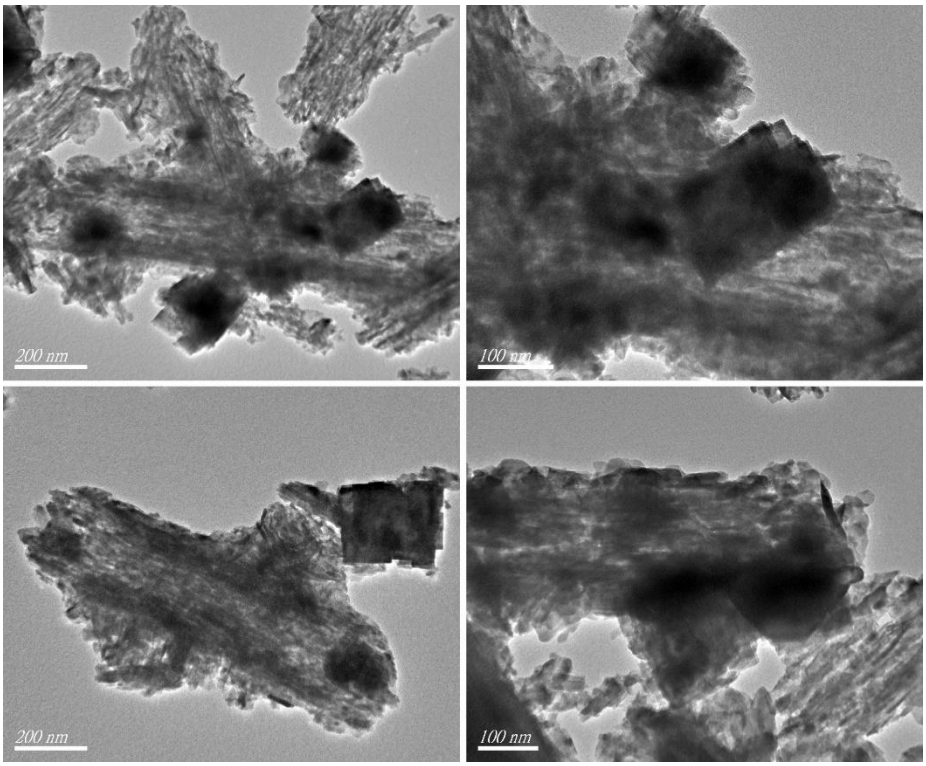

Fig. S8. TEM images of CuS/In_2S_3-4 after cycling.

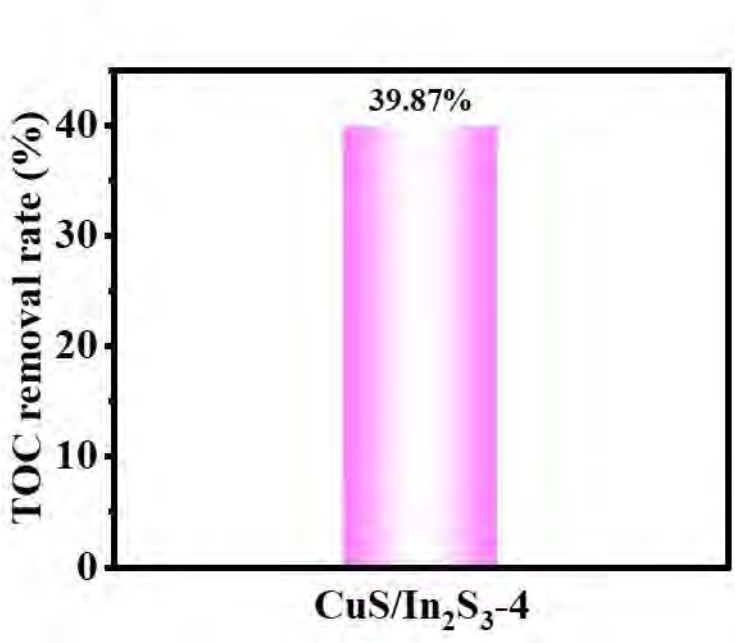

Fig. S9. TOC removal rate of CuS/In_2S_3-4 after light exposure for 90 min

Table S1 TOC values of MBT before and after light exposure for 90 min

sample	TOC (mg/L)
the MBT solution before degradation	5.2025
the MBT solution after degradation	3.1285

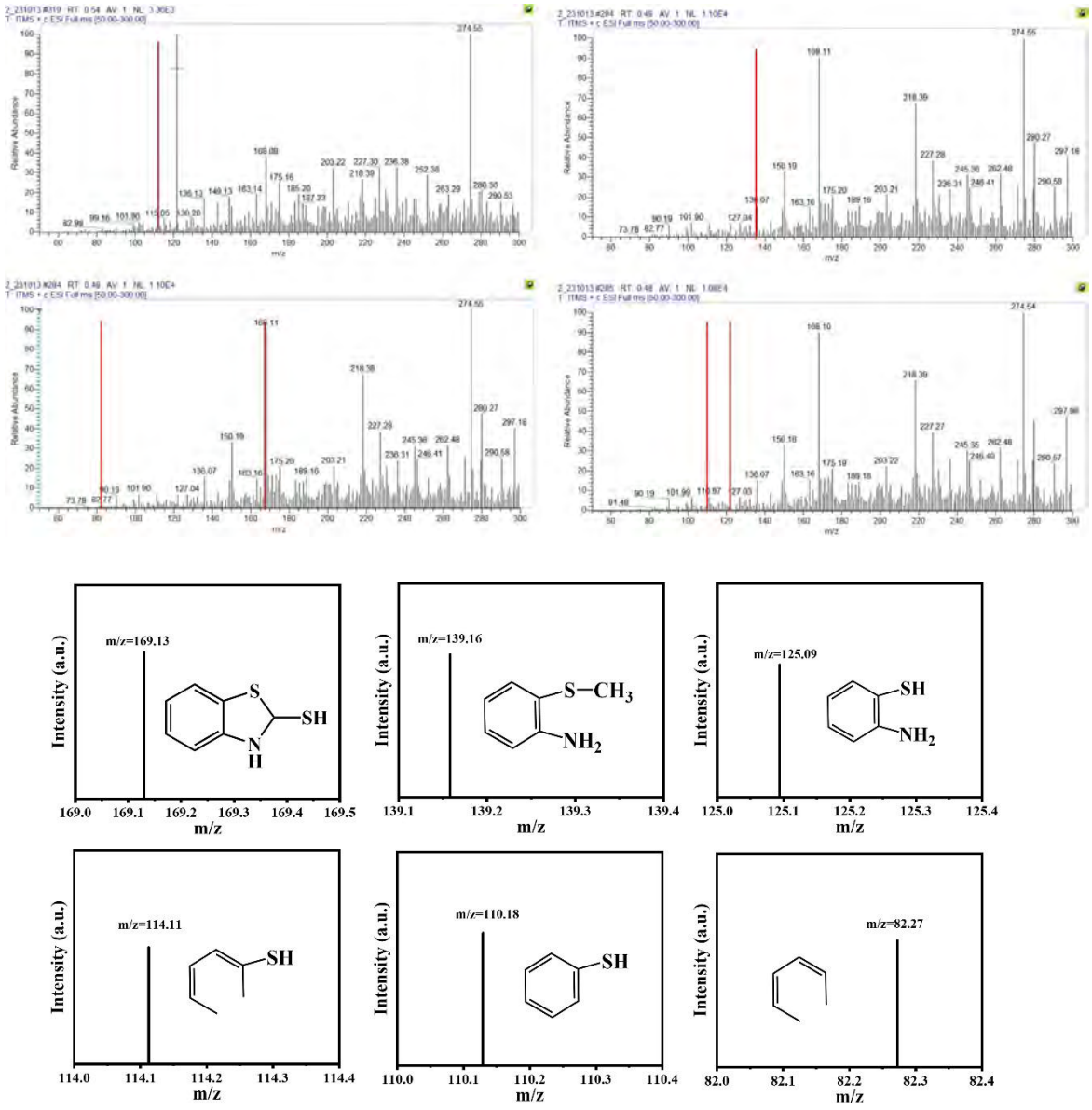

Fig. S10. The mass spectra of the solutions at different time points.